

Machine Learning for the identification of phase-transitions in interacting agent-based systems

Nikolaos Evangelou^{1,2}, Dimitrios G. Giovanis³,

George A. Kevrekidis^{2,4}, Grigorios A. Pavliotis⁶, Ioannis G. Kevrekidis^{1,2,*}

¹*Department of Chemical and Biomolecular Engineering,*

Johns Hopkins University, 3400 North Charles Street, Baltimore, MD 21218, USA

²*Department of Applied Mathematics and Statistics, Johns Hopkins University,*

3400 North Charles Street, Baltimore, MD 21218, USA

³*Department of Civil and Systems Engineering, Johns Hopkins University,*

3400 North Charles Street, Baltimore, MD, 21218, USA

⁴*Los Alamos National Laboratory, Los Alamos, NM, 87545, USA and*

⁵*Department of Mathematics, Imperial College London, London SW7 2AZ, United Kingdom**

Deriving closed-form, analytical expressions for reduced-order models, and judiciously choosing the closures leading to them, has long been the strategy of choice for studying phase- and noise-induced transitions for agent-based models (ABMs). In this paper, we propose a data-driven framework that pinpoints phase transitions for an ABM in its mean-field limit, using a smaller number of variables than traditional closed-form models. To this end, we use the manifold learning algorithm Diffusion Maps to identify a parsimonious set of data-driven latent variables, and show that they are in one-to-one correspondence with the expected theoretical order parameter of the ABM. We then utilize a deep learning framework to obtain a conformal reparametrization of the data-driven coordinates that facilitates, in our example, the identification of a single parameter-dependent ODE in these coordinates. We identify this ODE through a residual neural network inspired by a numerical integration scheme (forward Euler). We then use the identified ODE –enabled through an odd symmetry transformation– to construct the bifurcation diagram exhibiting the phase transition.

I. INTRODUCTION:

Complex dynamic phenomena are ubiquitous in natural sciences, social sciences, and engineering [1–4]. In many cases, their study has been performed using agent-based models (ABM) also known as interacting particle systems (IPS). The dynamics of those models in the thermodynamic (mean-field) limit undergo phase transitions – bifurcations in nonlinear dynamics terminology [5, 6]. The exploration of the dynamics of these systems typically involves extensive numerical simulation scenarios for a very large number, N , of interacting agents. However, extensive numerical simulations of huge ensembles of agents –to explore the dynamics of such ABM– can be truly challenging and this impedes the widespread utilization of these models. Coarse-graining methodologies become, therefore, necessary in order to reduce this complexity. Reducing the dimensionality of an ABM can be achieved by defining collective variables that are capable of accurately describing the full dynamics of such large systems in terms of a relatively small number of observables [7–9]; or discovering those by data mining [10–12].

In our previous work [9], we developed and successfully tested a model reduction approach based on the cumulants of the single-agent probability distribution for such large ABM systems. The approach was inspired by the seminal work by Dawson [13], in which it was shown that the mean-field PDE of a Desai-Zwanzig (DZ) model

is equivalent to a countably infinite system of equations for the moments. Note that the fluctuations of the DZ model at the phase transition become non-Gaussian and persistent, characterized by critical slowing down. The proposed coarse-graining framework was based on an analytical closure methodology of the infinite hierarchy of equations for the moments or, equivalently, cumulants of the probability distribution of the infinite-dimensional system. The basic steps for building a reduced-order DZ model are: (i) Consider the mean-field ansatz by writing the N -particle distribution function, the solution of the N -particle Fokker-Planck equation, as the product of one-particle distribution functions $\rho(x, t)$ [14]. In the mean-field limit $N \rightarrow +\infty$, the probability distribution $\rho(x, t)$ satisfies the McKean-Vlasov PDE, a nonlinear and *nonlocal* (integrodifferential) Fokker-Planck type equation which is the generalization of the well known Vlasov equation [15], when the particle dynamics is driven by white noise. The mean-field approximation is the simplest closure scheme in the BBGKY hierarchy, an infinite system of equations that govern the evolution of correlations. However, such coarse-graining, even at the simplest, mean-field level of description, comes at the expense of introducing nonlocality and nonlinearity to the PDE that governs the evolution of the one-particle distribution function. (ii) Represent $\rho(x, t)$ either in terms of its moments (Desai-Zwanzig [13]) or in terms of its Fourier coefficients (Smoluchowski/noisy Kuramoto model [16]), obtaining thus an infinite system of ordinary differential equations (ODEs) that is exactly equivalent to the McKean-Vlasov PDE. Truncating the equations for the moments (or the Fourier coefficients),

* yannisk@jhu.edu

while choosing an appropriate closure scheme gives the reduced-order model described and analyzed in [9]. However, selecting the correct closure scheme for the truncated moments' system is the *trickiest* part of the coarse-graining procedure. Note also that such coarse-graining methodologies quite often rely on detailed knowledge of the dynamics, in particular of the interaction forces between the agents. This analytical approximation requires choosing the “correct” observable(s), the right level of observation/analytical closure, and –importantly– the level at which we attempt the closure. To overcome these constraints, this Letter proposes a data-driven framework for studying phase transitions of ABMs by (i) data-driven discovery of the observables, (ii) determining the level of closure, and (iii) identifying the reduced dynamics directly from data. To this end, we employ Diffusion Maps [17], a manifold learning algorithm, conformal autoencoders [18] and residual neural networks inspired by numerical integrators of ordinary differential equations [12, 19–22]. This allows us to circumvent the difficulties arising from the choice of an analytical model and the selection of its closure.

As an example, we apply our data-driven framework to the generalization of the DZ model with multiplicative noise considered in [9]; this very well-studied ABM model features a second-order (continuous) phase transition, which enables us to compare the performance of our data-driven approach with well known analytical/computational results. We emphasize, however, that our method is quite general, since it does not depend on the detailed features of the interaction, and can be applied to many different ABMs that exhibit phase transitions in the thermodynamic limit.

II. THE AGENT-BASED MODEL:

We consider a model describing an ensemble of N identical interacting agents subject to multiplicative noise. For this model, the agents are coupled via a mean reverting force and a second-order phase transition exists at a critical temperature that can be calculated analytically [9][Eqn. A12]. This transition appears as a bifurcation of the mean-field dynamics. The dynamics of each agent, x_i , are described by a stochastic differential equation (SDE) of the form

$$dx_i = \left[-x_i^3 + (\alpha + \nu\sigma_m^2)x_i - \theta(x_i - \bar{x}) \right] dt + \sqrt{\sigma^2 + \sigma_m^2 x_i^2} dW_i; \quad (1)$$

where σ is the bifurcation parameter, θ denotes the interaction strength, α is a parameter characterizing the amplitude of the multiplicative noise, ν corresponds to different mathematical prescriptions of the SDEs (Itô, Stratonovich etc.) and, σ_m is a rectifying parameter: when $\sigma_m \neq 0$ the phase-transition is pushed to higher values of σ . The agents are coupled through \bar{x} , which denotes the center of mass of the system (equal to the

first moment M_1). Furthermore, $dW_i, i = 1 \dots N$ denotes independent Brownian motions. The values of the parameters were set to $\alpha = 1$, $\theta = 4$, $\sigma_m = 0.8$, $\nu = \frac{1}{2}$, and $N = 12,000$ as in [9].

For this model, it was demonstrated in [9] that, away from the phase transition at $\sigma \cong 1.89$, the first moment, i.e., the order parameter of the system, is sufficient for an accurate description of the mean-field dynamics. As we get closer to the phase transition/the bifurcation, more moments need to be taken into account in order to accurately locate the bifurcation. More specifically, it was shown, by means of numerical experiments, that at least a four-moment truncation is necessary in order to predict the bifurcation/phase transition accurately. In this work, by observing the eigenvalues of the Jacobian at the steady state (based on the moments equation proposed in [9]) we confirm that a clear separation of time scales prevails in the neighborhood of the bifurcation, and that the long-term dynamics live in a one-dimensional manifold. Our goal here, discussed in the next section, is to find a data-driven parametrization of this one-dimensional manifold, and identify the dynamics on it.

III. DATA-DRIVEN FRAMEWORK:

The main steps of our proposed data-driven workflow, illustrated also in Figure 1, are as follows:

- (a) Start by sampling temporal snapshots of the agent distribution evolution through our ABM for multiple initial conditions and parameter values σ (see Section A 1 of the Appendix for details).
- (b) Compute histograms of the collected ABM data for each snapshot.
- (c) Apply the Diffusion Maps algorithm (described in Section A 2 of the Appendix) to the sampled histograms (and to their estimated moments) to discover a set of reduced (latent) variables in which the data can be embedded.
- (d) Use the Y-shaped conformal autoencoder (see A 4) to identify a *conformal reparametrization* of the latent variables, disentangling state variability from parameter variability.
- (e) Identify an one-dimensional ODE, dependent on a single latent variable from the Y-shaped conformal autoencoder; this employs a residual neural network templated on forward Euler numerical initial value solver (see A 5 for more details).
- (f) Construct the bifurcation diagram that detects the phase transition by using the right-hand-side of the identified ODE (enhanced by a symmetry transformation).

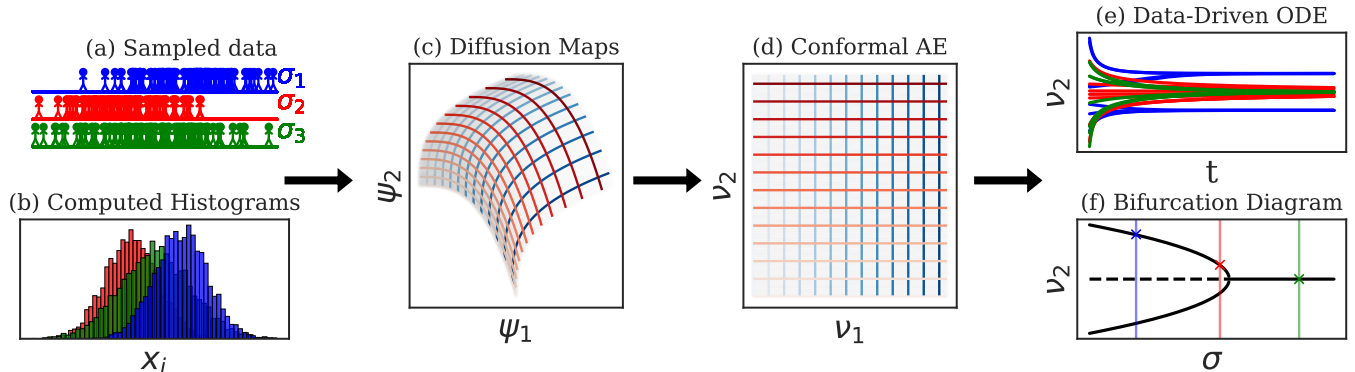


FIG. 1. Schematic of the overall workflow. (a) Sample data from the Agent-Based Model (ABM) across multiple initial conditions and parameter values, (b) Compute histograms for each snapshot of the ABM. (c) Apply the Diffusion Maps algorithm on the computed histograms to discover a reduced latent embedding. (d) Use a conformal autoencoder (AE) to find a conformal reparametrization of the latent space. (e) Identify a data-driven ODE in terms of the latent coordinate ν_2 of the AE. (f) Construct the bifurcation diagram in terms of the latent coordinate ν_2 .

IV. NUMERICAL RESULTS:

A. Latent data-driven coordinates

We start by sampling data on an equidistant grid 18 distinct values of the parameter σ in the interval $\sigma \in [0.5, 2.2]$. For each value of the parameter, we sample ~ 100 trajectories for different initial conditions. In Figure 2(a) we illustrate representative snapshots of the ABM model for three values of the parameter σ in the form of histograms. A more detailed description of the sampling strategy is discussed in Section A 1.

Given the sampled data from the ABM we compute the first four moments M_1, M_2, M_3, M_4 as

$$M_k = \frac{1}{N} \sum_{i=1}^N x_i^k(t) \quad (2)$$

where x_i^k denotes the i -th agent at a fixed time raised in the power k , M_k is the k -th moment of the population. The choice of four moments was based on our previous work [9] where we showed that a closed-form system of four coupled ODEs for the four moments can provide accurate predictions of the phase transition. This is further supported by studying the time-scale separation between the four-moment truncation and higher-order moment truncations of the dynamics, see B 1 in the Appendix. In Figure 2(b) we plot the first two moments M_1 and M_2 colored with the parameter σ . Based on this, we argue that the data are at least two-dimensional, and that the parameter σ appears to correlate with the moments M_1, M_2 .

We then proceed by computing Diffusion Maps (see Section A 2 for a description of the algorithm) using data from the sampled ABM simulation. The Diffusion Maps

algorithm was computed using: (a) histograms obtained for a single value of the parameter σ , (b) histograms obtained across our grid of 18 distinct σ values, (c) on the four computed moments from data sampled across our 18 values of σ . For the first case of a single value of σ , Diffusion Maps discovered a one-dimensional manifold. For the last two cases, a two-dimensional manifold was discovered; we elaborate more about each case below.

Computing Diffusion Maps for a single value of σ (based on histograms) gave a one-dimensional manifold parametrized by ψ_1 . We provide the details for the Diffusion Maps computation in Section A 2 a. We provide additional results in Section B 2 of the Appendix to support our argument that the data sampled at a single value of the parameter live on a one-dimensional manifold. In Figure 2(c) we plot the leading Diffusion Maps coordinate ψ_1 against the first moment M_1 and demonstrate that they are one-to-one. This suggests that Diffusion Maps is capable of discovering a coordinate that is one-to-one with the known order parameter M_1 for this model [9, 13, 24]. In Section B 2 of the Appendix we illustrate the relation of the Diffusion Maps coordinate with the subsequent moments M_2, M_3, M_4 .

We proceed with the Diffusion Maps computation on data sampled over multiple parameter values of σ . Details for the Diffusion Maps algorithm applied on histograms are provided in Section A 2 a. Here in Figures 2(d), 2(e) we show the two, non-harmonic eigenvectors that parametrize different eigendirections ψ_1 and ψ_2 colored with the parameter σ and the first moment M_1 . The selection of the non-harmonic eigenvectors was made by using the local linear regression algorithm proposed in [23] and implemented by the *datafold* Python package [25]. The residual r_k of the first two eigenvectors, shown in Figure 2(f), is greater than the residual of the remain-

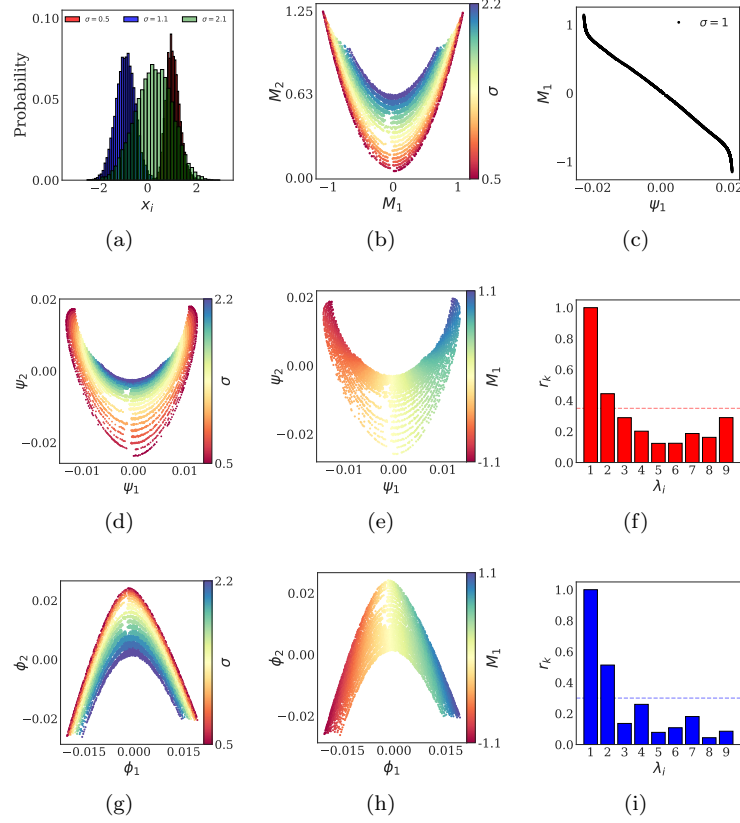


FIG. 2. (a) Representative histograms from snapshots of the ABM simulations for $\sigma = 0.5, 1.1, 2.2$. (b) The first two moments (M_1, M_2) estimated from the ABM simulations colored with the parameter value σ at which they were obtained. (c) One-to-one relation between leading histogram moment M_1 and leading Diffusion Maps coordinate. (d-f) Diffusion Maps on collected histograms from the ABM simulation: (d-e) show the non-harmonic diffusion map coordinates (ψ_1, ψ_2) colored with σ and M_1 respectively; (f) shows the residual (r_k) based on the local linear regression algorithm [23] indicating that ψ_1 and ψ_2 might be enough to parametrize the data (larger values of r_k). (g-i) Diffusion Maps on the first four moments $M_1 - M_4$ estimated from collected data of the ABM. The non-harmonic coordinates ϕ_1 and ϕ_2 colored with σ and M_1 . The r_k in (i) also indicates ϕ_1 and ϕ_2 are the two non-harmonic coordinates.

ing eigenvectors. This suggests that the first two eigenvectors (ψ_1, ψ_2) are non-harmonic, while the remaining ones are harmonic (functions) of the first two.

The Diffusion Maps algorithm applied using the computed first four moments reveals a two-dimensional manifold embedded in four dimensions. The first two eigenvectors in this case ϕ_1 and ϕ_2 , shown in Figures 2(g) and 2(h) are the non-harmonic, eigenvectors that parametrize the data. This is corroborated by the larger residuals r_k of the first two eigenvectors shown in Figure 2(i). Also in this case, the parameter σ and the first moment M_1 appear visually as functions of the Diffusion Maps coordinates (Figures 2(g) and 2(h)).

The Diffusion Maps results suggest that the mean-field dynamics of the ABM live on a two-dimensional manifold. However, the parameter σ appears to correlate with the behavior of the moments observed at that σ value. This suggests, that even though the data can be parametrized by two coordinates ψ_1, ψ_2 (or ϕ_1 and ϕ_2) one might be able to *disentangle* this coupled

two-dimensional description into a factorized (a single state) \times (a parameter) description. In the next section, we illustrate how a data-driven reparametrization of the Diffusion Maps coordinates can be achieved that will allow us to *disentangle* the effect of the parameter σ from that of the latent variable.

B. Y-shaped conformal autoencoder

In this section, we illustrate the use of the Y-shaped conformal autoencoder, originally introduced in our previous work [18] as a means of disentangling the effect of different parameter combinations on model outputs in the context of parameter nonidentifiability. The Y-shaped conformal autoencoder seeks a reparametrization of the Diffusion Maps coordinates in which it disentangles the effect of the parameter σ from that of the latent coordinates of the autoencoder. A more detailed description of the overall framework, the different loss function

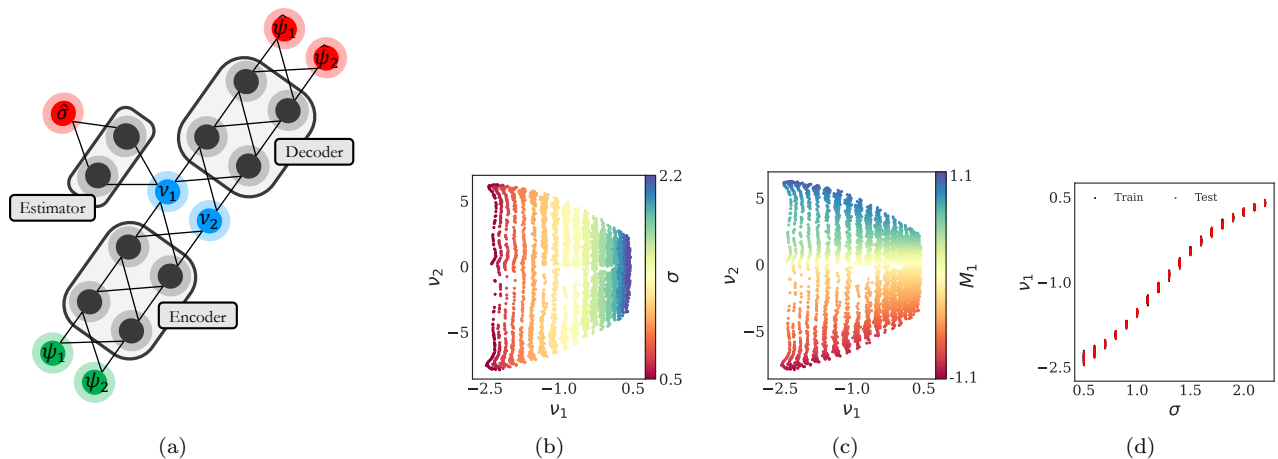


FIG. 3. (a) A schematic of the Y-shaped conformal autoencoder. The inputs to the network (ψ_1 and ψ_2) are shown as green nodes. The outputs of the autoencoder ($\hat{\psi}_1$ and $\hat{\psi}_2$) and the estimator are shown as red nodes. The latent variables (ν_1 and ν_2) are shown as light blue nodes. (b-c) The obtained latent coordinates ν_1, ν_2 colored with σ and M_1 respectively. (d) The parameter σ is plotted against the latent coordinate ν_1 indicating a strong dependence.

components of the network, and the training procedure we followed are discussed in Section A 4. A schematic of the Y-shaped conformal autoencoder is shown in Figure 3(a).

The coordinates ψ_1 and ψ_2 , obtained by computing the Diffusion Maps algorithm on estimated histograms of the ABM, were the ones used as input to the Y-shaped conformal autoencoder. The pair of coordinates ϕ_1, ϕ_2 obtained by Diffusion Maps on moments could have been used instead here, but we omit this for brevity.

The bottleneck latent variables ν_1, ν_2 are shown in Figures 3(b) and 3(c) colored with the parameter σ and the first moment M_1 . The parameter σ appears to be varying along ν_1 and M_1 along ν_2 . The latent variable ν_1 shows a strong correlation with the parameter σ , as depicted by Figure 3(d), indicating that they are effectively one-to-one. This reparametrization of the latent coordinates is crucial since, as we show in the next section, it allows us to identify a single-state dimension ODE depending on σ (rather than a needlessly two-dimensional ODE).

In Section A 4 we provide additional results obtained for the Y-shaped autoencoder illustrating the reconstruction of its input data (ψ_1, ψ_2). Remarkably, in addition, the Y-shaped autoencoder allows us to estimate σ from new, previously unseen histogram observation through ν_1 .

C. Identifying parameter dependent ODEs

Using the latent variable ν_2 obtained from the Y-shaped conformal autoencoder, we now identify a σ -dependent ODE; remember that ν_2 is conformal to ν_1 (and therefore, to σ). The identification of the parameter-dependent ODE was achieved through a residual neural network inspired by the forward Euler numer-

ical integration scheme. A schematic of the neural network is shown in Figure 4. The inputs to this network are the state variable at time t , $\nu_2(t)$, and the parameter σ , and the output is the state variable evolved to time $t + h$, $\nu_2(t + h)$. We provide a more detailed description of the forward Euler network and the constructed loss function scheme in Section A 5.

We test the ability of the ODE to produce accurate paths (trajectories), in ν_2 space, for unseen values of the parameter σ . We contrast the trajectories of the identified ODE with ground truth trajectories obtained by integrating the full ABM model (embedded in ν_2). In Figure 4(b) we provide a visual comparison between these two types of trajectories for three *unseen* values of the parameter σ . The paths generated by the ABM and those generated by the neural network-identified ODE show excellent visual agreement across different values of σ and different initial conditions. This suggests that the identified right-hand-side provides a successful approximation of the ground-truth dynamics.

D. Bifurcation Diagram: phase transition

In this section, we now proceed to test whether the parameter-dependent ODE identified in a data-driven way through our neural network can qualitatively and quantitatively capture the phase transition. More precisely, given the identified right-hand-side, we compute the steady-states across a range of values of the parameter σ and construct the bifurcation diagram. For values of $\sigma \in (0.5, 2.2)$ the constructed bifurcation diagram is shown in Figure 5(a). The bifurcation diagram shows that the model identifies the existence of three steady states, two stable and one unstable, for $\sigma < 1.84$. For $\sigma \geq 1.84$ a unique stable steady state exists. However,

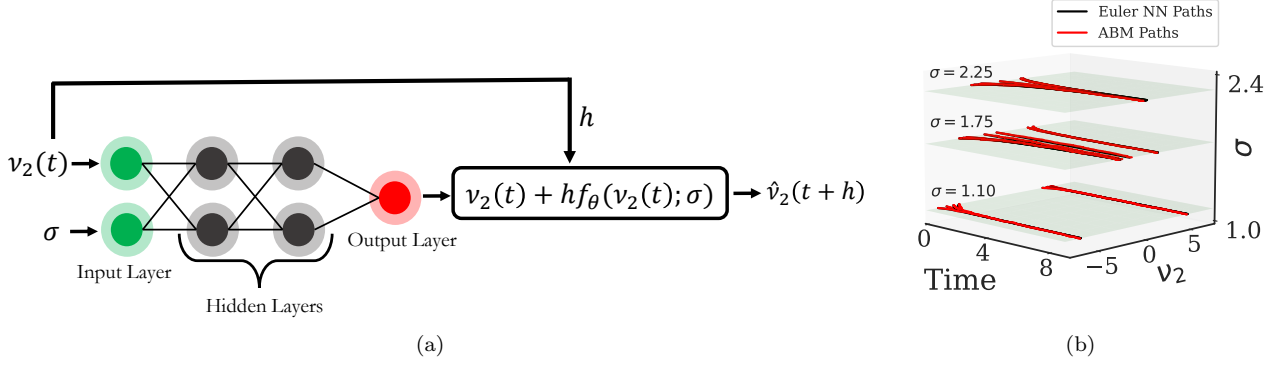


FIG. 4. (a) A schematic of the forward Euler residual neural network. The state variable $\nu_2(t)$, the parameter σ , and the time step h are inputs to the neural network that estimates the right-hand side f_θ of the ODE. The right-hand-side is then used to estimate the state variable $\hat{\nu}_2(t+h)$ by using a forward Euler step. (b) For unseen values of the parameter σ we contrast generated paths by the ODE with paths simulated by the ABM embedded in ν_2 .

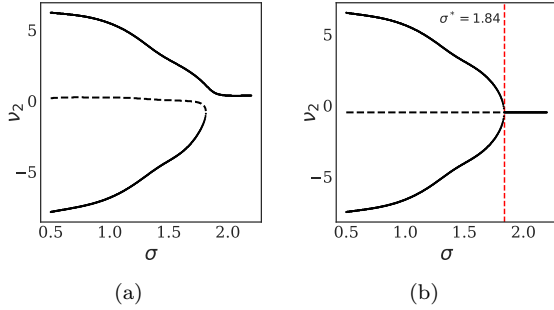


FIG. 5. (a) The bifurcation diagram constructed by the identified right-hand-side of the Euler neural network suggests a “perturbed” pitchfork. (b) The constructed bifurcation diagram by applying equation (3) to the identified right-hand-side shows a symmetric pitchfork.

the computed bifurcation diagram clearly possesses the flip symmetry of the generic pitchfork bifurcation. We have identified a *perturbed* pitchfork, in which the upper branch remains permanently stable and the lower branch exhibits a turning point where a stable and an unstable component collide.

To recover a generically symmetric pitchfork bifurcation diagram, a simple transformation suffices: given the identified right-hand-side $f_\theta(\nu_2(t); \sigma)$ of the neural network we compute

$$g(\nu_2; \sigma) = \frac{f_\theta(\nu_2(t); \sigma) - f_\theta(-\nu_2(t); \sigma)}{2}. \quad (3)$$

The vector field $g(\nu_2; \sigma)$ is then used to construct the bifurcation diagram, shown in Figure 5(b) correctly capturing the symmetry. Note that the computation of Equation (3) does not require a second neural network but only evaluations of the trained Euler neural network discussed in the previous section.

The critical parameter of the identified ODE occurs at $\sigma^* = 1.84$; the true critical transition has been com-

puted to be at $\sigma^* = 1.89$ [9]—see also [13][Eqn. 3.52] for the case of additive noise. This suggests that the identified ODE provides a qualitatively correct and arguably quantitatively accurate approximation of the phase transition.

V. SUMMARY AND CONCLUSIONS

We presented a data-driven framework for identifying qualitatively and approximating quantitatively phase transitions of interacting agent systems through an interplay between direct simulations and machine-learning-assisted, coarse-grained system identification and bifurcation analysis. We demonstrated that our framework is capable of identifying the phase transition of the Desai-Zwanzig system with a single, interpretable data-driven variable, in contrast to the derived closed-form model, proposed in [9] where a system of four approximate ODEs were required for the task. To discover the effective coarse (collective) variables that parameterize collected data from the ABM, the Diffusion Maps manifold learning algorithm [17] was used. We showed that, for a constant parameter value ($\sigma = 1$), away from the phase transition, the Diffusion Maps algorithm discovers a one-dimensional manifold parametrized by the data-driven coordinate ψ_1 ; and that ψ_1 is one-to-one with the theoretical order parameter M_1 . The nature of the Diffusion Maps results was not affected by whether the data were compared either (a) as histograms from the ABM simulations or (b) as a summary of the histograms in terms of the leading moments M_1, M_2, M_3, M_4 .

We then illustrated that, while data collected over a range of parameter values (bracketing the critical value) lie on a two-dimensional manifold, this manifold can be “disentangled” (factored) into a one-dimensional state-variability manifold “cross” a one-dimensional parameter variability manifold. To disentangle the variability due to the parameter σ from the state variability, in terms of

the latent Diffusion Maps coordinates (ψ_1, ψ_2) , we introduced a Y-shaped conformal autoencoder, initially proposed in [18] for addressing parameter non-identifiability. We illustrated that the autoencoder’s latent variables (ν_1, ν_2) form a conformal set of coordinates that ultimately allow us to learn a single effective nonlinear ODE, in terms of a single state variable ν_2 and depending on a single parameter σ (the latter being one-to-one with ν_1). This effective nonlinear ODE was identified via a residual neural network, templated on the forward Euler numerical integrator. We compared generated paths of the identified ODE for test values of the parameter σ to paths generated with the full ABM embedded in the latent coordinate ν_2 and demonstrated good agreement between the two. To construct the bifurcation diagram from the identified right-hand-side of the ODE, we used an odd symmetry transformation of the right-hand-side. This transformation provides a symmetric vector field and captures the pitchfork bifurcation that denotes the phase transition. Imposing known physical symmetries in the data-driven models in order to enhance accuracy and improve generalizability is currently an active area of research [26–34].

Our proposed, framework can be extended to a broad class of complex, multiscale dynamical systems for which a fine scale, atomistic/stochastic mode exists, but for which accurate closed form macroscopic equations at the coarse-grained level are not explicitly known. We are particularly interested in models from the social sciences, where no physics-informed natural choice for the order parameter(s) exists. As an example, we mention the noisy Hegselmann-Krause model for opinion dynamics [35], for which it has been rigorously proved that a discontinuous disorder (no consensus)/order (consensus) phase transition exists [6][Prop. 6.2]. It would be interesting to identify the phenomenological order parameter introduced in [35] using our approach. Other examples for which our approach is expected to be applicable are the Keller-Segel model for chemotaxis, see the work in [36–39], the Fitzhugh–Nagumo from Lattice Boltzmann in [40, 41], and the mean-field Fitzhugh–Nagumo model for Neurons [42][Sec. 5.6].

Returning to our illustrative example, we note again that the mean-field description of an ABM does not provide us with complete information about the dynamics, since fluctuations are ignored. This becomes particularly important close to transition points, where the fluctuations become persistent. In fact, the limits as N goes to infinity and as the temperature approaches the critical temperature *do not commute* [43]. As a consequence, correlations between particles—that decay exponentially fast away from the phase transition—cannot be ignored. This implies that, for an accurate description of the dynamics close to a phase transition, a single evolution equation for the single-particle density, e.g. the McKean-Vlasov PDE, is not sufficient, and has to be augmented by auxiliary equations for pair- and higher order correlations. Alternatively, we have to consider the

Dean-Kawasaki stochastic PDE [44, 45], that takes into account finite-particle effects and fluctuations. We leave this topic for future work.

ACKNOWLEDGMENTS

I.G.K. acknowledges partial support from the US AFOSR FA9550-21-0317 and the US Department of Energy SA22-0052-S001. G.A.P. is partially supported by the Frontier Research Advanced Investigator Grant ERC grant Machine-aided general framework for fluctuating dynamic density functional theory. The authors are grateful to N. Zagli and A. Zanonì for useful discussions for making available the code from [9] and [42], respectively. Many thanks to T. Gaskin for helping set up the collaboration with Imperial College London. He acknowledges the hospitality of the Johns Hopkins group.

CODES

The code used to generate the results for this paper will be made available in a public repository at https://gitlab.com/nicolasevangelou/ml_phase_transition upon acceptance of the paper.

Appendix A: Methods:

1. Data Collection

Given the ABM model described in Section II in the main text, we generated trajectories at 18 equidistant values of $\sigma \in [0.5, 2.2]$ [9]. For each value of σ we sampled 100 trajectories for different initial conditions (agents’ distribution) drawn from the Pearson distribution (implemented in Matlab) with prescribed mean, standard deviation, skewness, and kurtosis. The values for the mean, standard deviation, skewness, and kurtosis were chosen randomly from a prescribed grid of equidistant points: The mean was chosen from the range $[-2.0, 2.0]$, with increments of 0.2. The standard deviation was selected from the range $[0.0, 2.0]$, with increments of 0.1. The skewness was chosen from the range $[-2.0, 2.0]$, with increments of 0.2 and the kurtosis was selected from the range $[0.0, 15]$, with increments of 0.72. This scheme ensured a dense sampling both, in parameter and state space.

The integration time of the ABM, containing $N = 12,000$ agents, was set to $t_f = 10$ with a time-step $dt = 0.005$. Data were collected every five snapshots which led to a total of 400 snapshots per trajectory. Therefore, for a single value of the parameter, the total number of initial data is $N = 40,000$ (400×100) while for multiple values of the parameter $N = 720,000$ ($400 \times 100 \times 18$). Note that a number of trajectories

explodes and thus, are omitted from any further computations.

An additional preprocessing step was applied to the data before the Diffusion Maps computation that includes discarding a short transient t_{cut} for each trajectory. This ensures that the fast transients have decayed and the collected data contains only the long-term dynamics (that live on the slow manifold). When dealing with multiple parameter values we chose $t_{cut} = 1$ while for a single value of the parameter $\sigma = 1$ we choose $t_{cut} = 0.5$ to make sure that enough transients are close to the unstable steady state, otherwise, the manifold would appear as two clusters. As a test set, we sampled trajectories for three values of $\sigma = (1.11, 1.75, 2.25)$, not included in the training set. Those trajectories allowed for evaluating the performance of the ODE.

2. Diffusion Maps

The Diffusion Maps algorithm, introduced by Coifman and Lafon [17] can be used to discover a low-dimensional parameterization of high-dimensional data $\mathbf{X} = \{\mathbf{x}_i\}_{i=1}^N$ with each $\mathbf{x}_i \in \mathbb{R}^m$. Diffusion Maps constructs a weighted graph $\mathbf{K} \in \mathbb{R}^{N \times N}$ between the sampled data points by using a kernel function. A common choice, also used in our case, is the Gaussian kernel

$$K(\mathbf{x}_i, \mathbf{x}_j) = \exp\left(\frac{-\|\mathbf{x}_i - \mathbf{x}_j\|_2^2}{2\varepsilon}\right), \quad (\text{A1})$$

where ε is a positive hyperparameter that controls the rate of the kernel's decay. The metric $\|\cdot\|$ in our case was chosen as the ℓ^2 norm but different metrics are also possible.

To discover a low-dimensional manifold, regardless of the sampling density, the following normalization is required

$$\tilde{\mathbf{K}} = \mathbf{P}^{-1} \mathbf{K} \mathbf{P}^{-1} \quad (\text{A2})$$

where $P_{ii} = \sum_{j=1}^m K_{jj}$. A second normalization of $\tilde{\mathbf{K}}$ recovers a row-stochastic, Markovian matrix

$$\mathbf{M} = \mathbf{D}^{-1} \tilde{\mathbf{K}} \quad (\text{A3})$$

where \mathbf{D} is a diagonal matrix defined as $D_{ii} = \sum_{j=1}^N \tilde{K}_{ij}$. The entries of matrix \mathbf{M} can be seen as probabilities of jumping from one point to the other. The eigendecomposition of \mathbf{M} ,

$$\mathbf{M} \phi_i = \lambda_i \phi_i, \quad (\text{A4})$$

provides a set of eigenvectors ϕ_i and corresponding eigenvalues λ_i . To obtain a more parsimonious representation of the original data set \mathbf{X} proper selection of the eigenvectors is needed. If the *intrinsic* dimension of the data is

small, this selection can be achieved by visual inspection of the non-harmonic eigenvectors (eigenvectors that span independent directions) [46]. Alternatively, the local-linear regression algorithm proposed by Dsilva et al. [23] can be used for selecting the non-harmonic eigenvectors. If, the number of independent non-harmonic eigenvectors is smaller than the dimension m of the data \mathbf{X} , then dimensionality reduction has been achieved. In our work, the Python library *datafold* [25] was used for the Diffusion Maps and the local-linear regression algorithms.

a. Diffusion Maps on ABM data

In this section, we provide details on how the Diffusion Maps algorithm was computed on computed histograms and computed moments from the ABM. In the first case, for each snapshot of the ABM we constructed a histogram as an approximation of the agents' density. Each histogram contains 40 equidistant bins defined in the range $[-4, 4]$. This range ensures that all agents in the collected (training) data lie in between. Note, that the method is insensitive to the selected number of bins. To reduce the computational cost of the Diffusion Maps, we subsampled the training data uniformly [25] which resulted in $N \sim 3,500$ when Diffusion Maps applied for a single parameter and $N \sim 19,000$ for multiple values of the parameter. The hyperparameter ε was selected as the square of the median of the pairwise distances multiplied by a constant c , where $c = 0.03$ for a single value of the parameter σ and $c = 20$ for multiple values of the parameter σ . In the second case, Diffusion Maps was computed on the sampled moments, M_1, M_2, M_3, M_4 . Again, to alleviate the computational cost we subsampled the data [25], which results in $N \sim 11,000$. The hyperparameter ε was also selected for this case by computing the median of the pairwise distances multiplied with $c = 10$.

3. Nyström Extension

The Nyström Extension formula provides a numerical approximation of eigenfunctions of the form [47]

$$\int_a^b M(\mathbf{x}_j, \mathbf{x}_i) \phi_i(\mathbf{x}_i) d\mathbf{x}_i = \lambda \phi(\mathbf{x}_j). \quad (\text{A5})$$

In our work, Nyström extension is utilized when new *out-of-sample* data points are given, e.g., $\mathbf{x}_{new} \notin \mathbf{X}$. To generate the Diffusion Maps coordinates ϕ_{new} Nyström extension uses an interpolation scheme based on the kernel computations and normalizations applied during the dimensionality reduction step, discussed in the previous Section. The Nyström extension formula reads

$$\phi_i(\mathbf{x}_{new}) = \frac{1}{\lambda_i} \sum_{j=1}^N \tilde{\mathbf{M}}(\mathbf{x}_{new}, \mathbf{x}_j) \phi_i(\mathbf{x}_j), \quad (\text{A6})$$

where $\phi_i(x_{new})$ denotes the estimated i -th eigenvector for the data point ϕ_{new} , λ_i denotes the corresponding eigenvalue, $\phi_i(x_j)$ denotes the j -th component of the i -th eigenvector and $\tilde{\mathbf{M}}(\cdot, \cdot)$ denotes the kernel function used to determine the similarity of x_{new} to all the points in \mathbf{X} .

4. Y-shaped conformal autoencoder

The Y-shaped conformal autoencoder was initially presented in [18]. In this work, the Y-shaped conformal autoencoder consists of the three connected (sub)networks

$$\text{Encoder} : (\psi_1, \psi_2) \mapsto (\nu_1, \nu_2) \quad (\text{A7})$$

$$\text{Decoder} : (\nu_1, \nu_2) \mapsto (\hat{\psi}_1, \hat{\psi}_2) \quad (\text{A8})$$

$$\text{Estimator} : \nu_1 \mapsto \hat{\sigma}. \quad (\text{A9})$$

The Encoder receives as inputs the two Diffusion Maps coordinates ψ_1, ψ_2 and maps them to the latent variables ν_1, ν_2 . The Decoder aims to reconstruct the Diffusion Maps coordinates from the latent variables ν_1, ν_2 . The Estimator has as input the latent coordinate ν_1 and aims to learn a map from ν_1 to the parameter σ .

The loss function used to train the Y-shaped conformal autoencoder consists of three parts: (a) The loss function of the Encoder-Decoder (autoencoder) \mathcal{L}_{ae} that aims to reconstruct the input itself (b) the loss function of the Estimator, $\mathcal{L}_{est.}$, that aims to reproduce the parameter σ given ν_1 and (c) the loss function for imposing the conformality constrain, $\mathcal{L}_{con.}$, between ν_1 and ν_2 ,

$$\langle \nabla \nu_1, \nabla \nu_2 \rangle = 0 \quad (\text{A10})$$

where the gradient ∇ is in terms of the Diffusion Maps coordinates (ψ_1, ψ_2) of the input and $\langle \cdot, \cdot \rangle$ denotes the inner product between the two vectors. The gradients were computed by using the automatic differentiation of Pytorch [48]. In practice, instead of using equation A10, one can minimize the angle between the vectors

$$\cos\theta(\nabla \nu_1, \nabla \nu_2) = \frac{\nabla \nu_1 \cdot \nabla \nu_2}{\|\nabla \nu_1\| \|\nabla \nu_2\|} \quad (\text{A11})$$

which stabilizes the training of the network. We describe details for training the network, specifics about the architecture used, and the choice of hyperparameters in the next section.

a. Hyperparameter selection and training procedure

The implementation of the Y-shaped conformal autoencoder was done with the Pytorch Python library [48].

Each (sub)network (Encoder, Decoder, Estimator) in the architecture of the Y-shaped conformal autoencoder

consists of five fully connected layers. The first four hidden layers have 20 neurons and $\tanh(t)$ activation functions and the fifth has no activation function (linear activation) and its size depends on the size of the desired output. The ADAM optimizer was chosen for training the overall network. We chose mini-batches of size 32 to train the network. The learning rate was selected as $\eta = 0.001$ and the number of epochs as $\text{epochs} = 500$. Training the network for a larger number of epochs leads to overfitting.

To train the network and test its generalization capability we used $\sim 19,000$ data points. We split the data into train|test|validation as 80:10:10. We then rescaled the training data by using the *MinMaxScaler* Python preprocessing scheme from *sklearn*. We applied the same transformation for the validation and test sets. During the training of the network, we used only the training set to perform backpropagation and the validation set to get insight into the model's performance. The network did not see the test set during training.

The optimization process we performed was *heuristic*: for a fixed mini-batch two updates (backpropagation steps) were performed. The first step updates the weights of the Encoder-Decoder and the second step the weights of the Estimator-Encoder. Altering this training protocol is possible. In Algorithm 1 below we provide a more detailed description of the network's training.

Upon training of the neural network, the estimated MSE for the autoencoder's reconstruction, was $\mathcal{L}_{ae} = 1.36e - 08$ on the train set and $\mathcal{L}_{ae} = 1.37e - 08$ on the test set. The MSE for the Estimator was $\mathcal{L}_{est.} = 1.2e - 03$ for the train set and $\mathcal{L}_{est.} = 1.2e - 03$ for the test. The average value of the $\cos\theta$, on the train set was $\mathcal{L}_{con.} = 2.72e - 05$ and on the test set $\mathcal{L}_{con.} = 2.63e - 05$.

5. Forward Euler neural network

In this section, we describe how we identified the right-hand side of an ordinary differential equation directly from data. Let $\nu_2(t)$ be a state variable whose dynamics are governed by a σ -dependent ODE given by the general form

$$\dot{\nu}_2(t) = f(\nu_2(t); \sigma) \quad (\text{A12})$$

Our goal is to construct a neural network architecture inspired by numerical integrators of ODEs to estimate the right-hand-side $f(\nu_2(t); \sigma)$. To this end, we constructed a forward Euler residual neural network depicted in Figure 4. To train this network, we do not require long trajectories but only snapshots of the form $\mathcal{D} = \{\nu_2(t+h), \nu_2(t), \sigma, h\}$ where $\nu_2(t)$ is the state variable at time t , $\nu_2(t+h)$ is the state variable after a small time-step h . Given sampled data in the form of \mathcal{D} we wish to approximate f by using a neural network, with weights denoted as θ .

To formulate the loss used to train the network f_θ we remind the reader that the forward Euler approximates

Input: Diffusion Maps coordinates ψ_1, ψ_2 and parameter values σ .

Output: The weights of: (i) Encoder (θ_{encoder}), (ii) Decoder (θ_{decoder}), (iii) Estimator ($\theta_{\text{estimator}}$). For $i = 1, 2, \dots, T$

1. Predict:

$$\begin{aligned}(\nu_1, \nu_2) &= \text{Encoder}(\psi_1, \psi_2) \\ (\hat{\psi}_1, \hat{\psi}_2) &= \text{Decoder}(\nu_1, \nu_2)\end{aligned}$$

2. Compute Autoencoder (Encoder-Decoder) and Conformality Losses:

$$\begin{aligned}\mathcal{L}_1 &= \mathcal{L}_{\text{ae}} + \mathcal{L}_{\text{con}}. \\ &= \text{MSE}(\hat{\psi}, \psi) + \alpha \text{MSE}(\cos\theta(\nabla\nu_1, \nabla\nu_2), 0)\end{aligned}$$

3. Backpropagation step - update weights (illustration with gradient descent):

$$\begin{aligned}\theta_{\text{encoder}}^- &= \eta \theta_{\text{encoder}} \mathcal{L}_1 \\ \theta_{\text{decoder}}^- &= \eta \theta_{\text{decoder}} \mathcal{L}_1\end{aligned}$$

4. Predict:

$$\begin{aligned}(\nu_1, \nu_2) &= \text{Encoder}(\psi_1, \psi_2) \\ \hat{\sigma} &= \text{Estimator}(\nu_1)\end{aligned}$$

5. Compute Estimator Loss:

$$\mathcal{L}_{\text{est.}} = \text{MSE}(\hat{\sigma}, \sigma)$$

6. Backpropagation step - update weights (illustration with gradient descent)

$$\begin{aligned}\theta_{\text{estimator}}^- &= \eta \theta_{\text{estimator}} \mathcal{L}_{\text{est.}} \\ \theta_{\text{encoder}}^- &= \eta \theta_{\text{encoder}} \mathcal{L}_{\text{est.}}\end{aligned}$$

Algorithm 1: The algorithm illustrates a full iteration during training of the Y-shaped conformal autoencoder. We set the scale parameter to $\alpha = 10$. The learning rate is denoted as η .

the evolution of an ODE, by a small positive step h , as

$$\nu_2(t+h) = \nu_2(t) + hf(\nu_2; \sigma). \quad (\text{A13})$$

In our case, without having access to f but only data in the form \mathcal{D} we wish to approximate the right-hand-side with the neural network f_θ . This is achieved by performing for each pair of inputs $(\nu_2(t), \sigma)$ one integration step of size h , estimating the evolved dynamics $\hat{\nu}_2(t+h)$ and minimizing the loss

$$\mathcal{L}(\theta|\nu_2(t), \nu_2(t+h), h, \sigma) = \|\hat{\nu}_2(t+h) - \nu_2(t+h)\|^2. \quad (\text{A14})$$

For our computations, the time step h was kept constant but the overall approach can be easily extended to handle also varying time steps h .

a. Hyperparameter selection and training procedure

The implementation of the forward Euler neural networks was done with the Tensorflow/Keras Python libraries [49].

To train the forward Euler neural network we need to ensure our data is in the form of snapshots \mathcal{D} . To achieve that we used the Nyström extension formula (see Section A 3) to all the available sampled trajectories and obtained the corresponding trajectories in $\psi_1\psi_2$. We then evaluated the Encoder to get trajectories in terms of ν_2 . These two steps provided us with $\sim 600,000$ snapshots. We then split the data into train|test|validation as 80:10:10. We then centered and whitened the data (based on the mean and variance of the training set) and applied the same transformation to the validation and test set.

The architecture consisted of two hidden layers with 10 neurons each. The first hidden layer had a $\tanh(t)$ activation function and the second hidden layer had a linear activation function. We used ADAM to optimize this network. The mini-batch size was set to 32, the number of total epochs to 100, and the learning rate to $\eta = 0.001$. The learning curves for the training and validation are shown in Figure 9(a). The ability of the network to fit the training set and generalize is shown in 9(b). Upon training of the network, the MSE on the train and test sets were $2.63e-03$ and $2.79e-05$ respectively.

Appendix B: Additional Results

1. Separation of time scales

In this Section, we discuss the separation of time scales for the reduced order models based on the equations for the moments proposed in [9]. As shown in Figure 6 the slowest eigenvalue λ_1 is at least one order of magnitude smaller than the second slowest λ_2 . This suggests that the dynamics after a short transient are slaved in the direction of this slowest eigenvalue and are effectively one-dimensional.

2. Diffusion Maps

In this section, we provide additional results for the Diffusion Maps computation for $\sigma = 1$. We showed in the main text that the Diffusion Maps coordinate ψ_1 is one-to-one with the first moment M_1 . Here we show that M_3 is also one-to-one with ψ_1 (Figure 7(b)) and that the even moments M_2 and M_4 can be seen as functions of ψ_1 (Figures 7(a), 7(c)).

We also show that the residuals r_k computed with the local-linear regression algorithm [23] indicate that ψ_1 is enough to parametrize the data for this case; since the residuals for the remaining eigenvectors are much smaller. To strengthen, the argument that the manifold in this

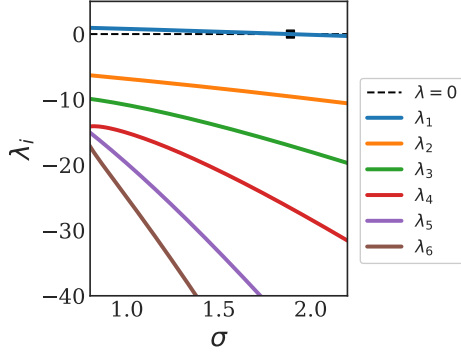


FIG. 6. The eigenvalues of the Jacobian computed across a range of parameter values σ for the moments' equations with six ODEs presented in [9]. The slowest eigenvalue λ_1 crosses the real axis at $\sigma = 1.89$ where the bifurcation occurs. The black square indicates the value of σ where the (slowest) eigenvalue crosses zero.

case is one-dimensional we show in Figure 7(e) the eigenvectors $\psi_2 - \psi_9$ plotted against the first non-trivial eigenvector ψ_1 . From Figure 7(e) it appears that the eigenvectors $\psi_2 - \psi_9$ are harmonics of ψ_1 . This suggests that the manifold for a fixed value of σ is one-dimensional.

3. Y-shaped conformal autoencoder

In this section, we provide additional results regarding the Y-shaped conformal autoencoder described in the main text. We illustrate in Figure 8(a) level sets as contour lines of ψ_1 and ψ_2 in terms of the latent coordinates ν_1, ν_2 . The ability of the Estimator to predict the parameter σ from ν_1 is shown in Figure 8(b) for train (black dots) and test (red dots) points. We also illustrate, in Figures 8(c), 8(d), the reconstruction of the autoencoder for train and test points.

4. Euler neural network

In this section, we provide some additional results for the forward Euler neural network. The learning curves for the training and validation are shown in Figure 9(a). The ability of the network to fit the train set and generalize is shown in Figure 9(b). Note that the normalized value of the state variable ν_2 is shown in Figure 4.

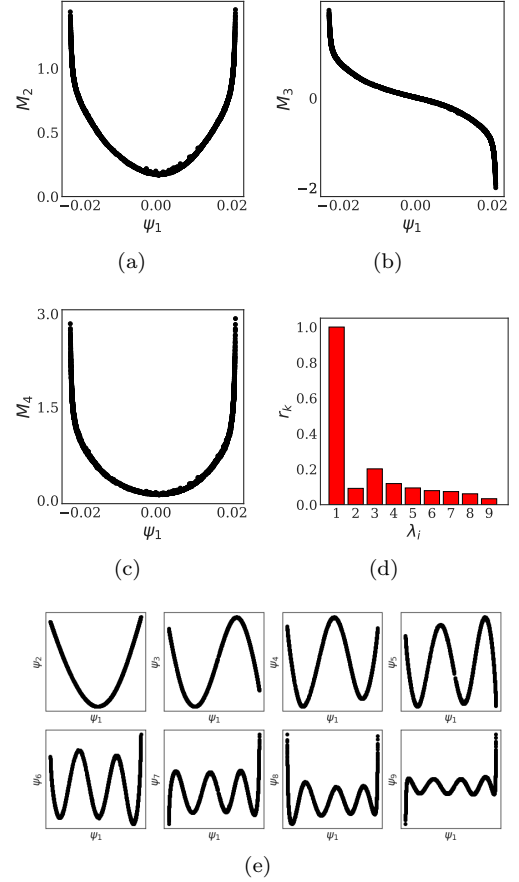


FIG. 7. (a-c) The Diffusion Maps coordinate ψ_1 is plotted against the computed moments M_2 , M_3 and M_4 respectively. (d) The residual r_k estimated by the local linear regression algorithm [23] indicates that the first eigenvector is enough to parameterize the data, with a higher value r_k . (e) The eigenvector ψ_1 is plotted against the eigenvectors $\psi_2 - \psi_9$. This supports our argument that the eigenvectors $\psi_2 - \psi_9$ are harmonics of ψ_1 .

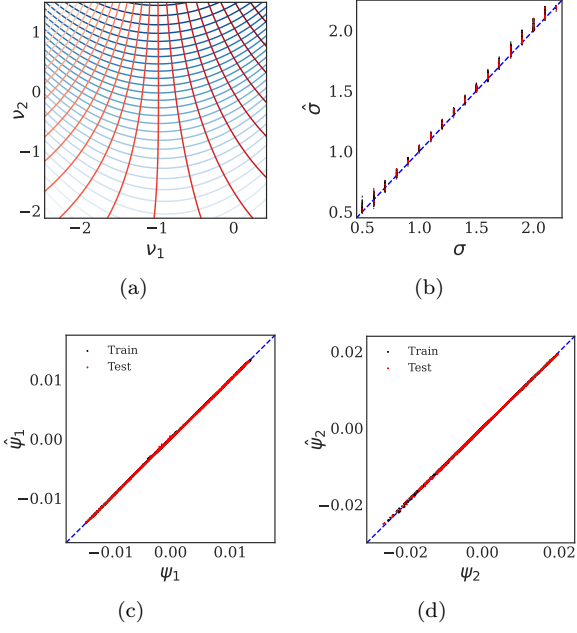


FIG. 8. (a) Level sets of the Diffusion Maps coordinates ψ_1 and ψ_2 in the latent coordinates of the autoencoder ν_1 ν_2 . (b) The true values of the parameter σ are plotted against the reconstructed by the Estimator for train (black) and test (red) points. The blue dashed line indicates $y = x$. (c-d) The true values of the Diffusion Maps coordinates ψ_1 and ψ_2 are plotted against the reconstructed $\hat{\psi}_1$, $\hat{\psi}_2$ coordinates by the autoencoder.

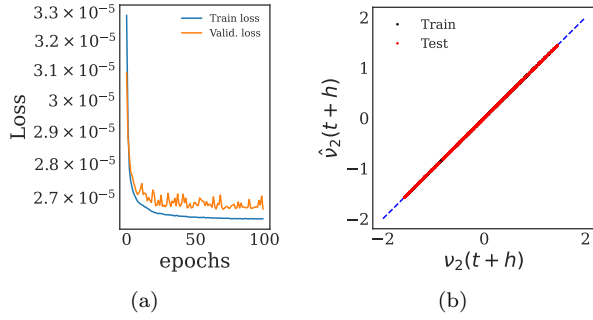


FIG. 9. (a) The learning curves for the train and validation sets. (b) The true values of the state variable $\nu_2(t+h)$ plotted against the predicted by the Euler neural network $\hat{\nu}_2(t+h)$ for the train (black points) and test (red points).

- [1] G. Naldi, L. Pareschi, and G. Toscani, *Mathematical modeling of collective behavior in socio-economic and life sciences* (Springer Science & Business Media, 2010).
- [2] L. Pareschi and G. Toscani, *Interacting multiagent systems: kinetic equations and Monte Carlo methods* (OUP Oxford, 2013).
- [3] L. Helfmann, J. Heitzig, P. Koltai, J. Kurths, and C. Schütte, Statistical analysis of tipping pathways in agent-based models, *The European Physical Journal Special Topics* **230**, 3249 (2021).
- [4] L. Helfmann, D. C.N., A. Djurdjevac, S. Winkelmann, and C. Schütte, From interacting agents to density-based modeling with stochastic PDEs, *Commun. Appl. Math. Comput. Sci.* **16**, 1 (2021).
- [5] L. Chayes and V. Panferov, The McKean-Vlasov equation in finite volume, *J. Stat. Phys.* **138**, 351 (2010).
- [6] J. A. Carrillo, R. S. Gvalani, G. A. Pavliotis, and A. Schlichting, Long-time behaviour and phase transitions for the McKean-Vlasov equation on the torus, *Arch. Ration. Mech. Anal.* **235**, 635 (2020).
- [7] T. Gross, C. J. D. D’Lima, and B. Blasius, Epidemic dynamics on an adaptive network, *Physical review letters* **96**, 208701 (2006).
- [8] S. Winkelmann, J. Zonker, C. Schütte, and N. D. Conrad, Mathematical modeling of spatio-temporal population dynamics and application to epidemic spreading, *Mathematical biosciences* **336**, 108619 (2021).
- [9] N. Zagli, G. A. Pavliotis, V. Lucarini, and A. Alecio, Dimension reduction of noisy interacting systems, *Physical Review Research* **5**, 013078 (2023).
- [10] P. Liu, H. R. Safford, I. D. Couzin, and I. G. Kevrekidis, Coarse-grained variables for particle-based models: diffusion maps and animal swarming simulations, *Computational Particle Mechanics* **1**, 425 (2014).
- [11] P. Liu, C. Siettos, C. W. Gear, and I. Kevrekidis, Equation-free model reduction in agent-based computations: Coarse-grained bifurcation and variable-free rare event analysis, *Mathematical Modelling of Natural Phenomena* **10**, 71 (2015).
- [12] G. Fabiani, N. Evangelou, T. Cui, J. M. Bello-Rivas, C. P. Martin-Linares, C. Siettos, and I. G. Kevrekidis, Tasks makyth models: Machine learning assisted surrogates for tipping points, *arXiv preprint arXiv:2309.14334* (2023).
- [13] D. A. Dawson, Critical dynamics and fluctuations for a mean-field model of cooperative behavior, *J. Statist. Phys.* **31**, 29 (1983).
- [14] N. Martzel and C. Aslangul, Mean-field treatment of the many-body Fokker-Planck equation, *J. Phys. A* **34**, 11225 (2001).
- [15] R. Balescu, *Statistical dynamics. Matter out of equilibrium* (Imperial College Press, London, 1997).
- [16] J. A. Acebrón, L. L. Bonilla, C. J. Pérez V., F. Ritort, and R. Spigler, The kuramoto model: A simple paradigm for synchronization phenomena, *Rev. Mod. Phys.* **77**, 137 (2005).
- [17] R. R. Coifman and S. Lafon, Diffusion maps, *Applied and computational harmonic analysis* **21**, 5 (2006).
- [18] N. Evangelou, N. J. Wichrowski, G. A. Kevrekidis, F. Dietrich, M. Kooshkbaghi, S. McFann, and I. G. Kevrekidis, On the parameter combinations that matter and on those that do not: data-driven studies of parameter (non) identifiability, *PNAS nexus* **1**, pgac154 (2022).
- [19] R. Rico-Martinez, K. Krischer, I. Kevrekidis, M. Kube, and J. Hudson, Discrete-vs. continuous-time nonlinear signal processing of cu electrodisolution data, *Chemical Engineering Communications* **118**, 25 (1992).
- [20] R. González-García, R. Rico-Martinez, and I. G. Kevrekidis, Identification of distributed parameter systems: A neural net based approach, *Computers & chemical engineering* **22**, S965 (1998).
- [21] F. Dietrich, A. Makeev, G. Kevrekidis, N. Evangelou, T. Bertalan, S. Reich, and I. G. Kevrekidis, Learning effective stochastic differential equations from microscopic simulations: Combining stochastic numerics and deep learning, *arXiv preprint arXiv:2106.09004* (2021).
- [22] N. Evangelou, F. Dietrich, J. M. Bello-Rivas, A. J. Yeh, R. S. Hendley, M. A. Bevan, and I. G. Kevrekidis, Learning effective sdes from brownian dynamic simulations of colloidal particles, *Molecular Systems Design & Engineering* (2023).
- [23] C. J. Dsilva, R. Talmon, R. R. Coifman, and I. G. Kevrekidis, Parsimonious representation of nonlinear dynamical systems through manifold learning: A chemotaxis case study, *Applied and Computational Harmonic Analysis* **44**, 759 (2018).
- [24] C. Van den Broeck, J. M. R. Parrondo, J. Armero, and A. Hernández-Machado, Mean field model for spatially extended systems in the presence of multiplicative noise, *Phys. Rev. E* **49**, 2639 (1994).
- [25] D. Lehmberg, F. Dietrich, G. Köster, and H.-J. Bungartz, Datafold: Data-driven models for point clouds and time series on manifolds, *Journal of Open Source Software* **5**, 2283 (2020).
- [26] P. J. Olver, Modern developments in the theory and applications of moving frames, *London Math. Soc. Impact150 Stories* **1**, 14 (2015).
- [27] M. Mattheakis, P. Protopapas, D. Sondak, M. Di Giovanni, and E. Kaxiras, Physical symmetries embedded in neural networks, *arXiv preprint arXiv:1904.08991* (2019).
- [28] D. Yarotsky, Universal approximations of invariant maps by neural networks, *Constructive Approximation* **55**, 407 (2022).
- [29] B. Blum-Smith and S. Villar, Equivariant maps from invariant functions, *arXiv preprint arXiv:2209.14991* (2022).
- [30] S. Villar, W. Yao, D. W. Hogg, B. Blum-Smith, and B. Dumitrescu, Dimensionless machine learning: Imposing exact units equivariance, *arXiv preprint arXiv:2204.00887* (2022).
- [31] P. J. Olver, M. Sabzevari, and F. Valiquette, Normal forms, moving frames, and differential invariants for non-degenerate hypersurfaces in c^2 , *The Journal of Geometric Analysis* **33**, 192 (2023).
- [32] P. Jin, Z. Zhang, A. Zhu, Y. Tang, and G. E. Karniadakis, Sympnets: Intrinsic structure-preserving symplectic networks for identifying hamiltonian systems, *Neural Networks* **132**, 166 (2020).
- [33] F. Alet, D. Doblar, A. Zhou, J. Tenenbaum, K. Kawaguchi, and C. Finn, Noether networks: meta-learning useful conserved quantities, *Advances in Neural Information Processing Systems* **34**, 16384 (2021).

- [34] J. W. Burby, Q. Tang, and R. Maulik, *Computing Poincaré maps using physics-informed deep learning*, Tech. Rep. (Los Alamos National Lab.(LANL), Los Alamos, NM (United States), 2020).
- [35] C. Wang, Q. Li, W. E, and B. Chazelle, Noisy Hegselmann-Krause systems: phase transition and the $2R$ -conjecture, *J. Stat. Phys.* **166**, 1209 (2017).
- [36] S. Lee, Y. M. Psarellis, C. I. Siettos, and I. G. Kevrekidis, Learning black-and gray-box chemotactic pdes/closures from agent based monte carlo simulation data, *Journal of Mathematical Biology* **87**, 15 (2023).
- [37] Y. M. Psarellis, S. Lee, T. Bhattacharjee, S. S. Datta, J. M. Bello-Rivas, and I. G. Kevrekidis, Data-driven discovery of chemotactic migration of bacteria via machine learning, *arXiv preprint arXiv:2208.11853* (2022).
- [38] C. I. Siettos, System level numerical analysis of a monte carlo simulation of the e. coli chemotaxis, *arXiv preprint arXiv:1011.1467* (2010).
- [39] S. Setayeshgar, C. W. Gear, H. G. Othmer, and I. G. Kevrekidis, Application of coarse integration to bacterial chemotaxis, *Multiscale Modeling & Simulation* **4**, 307 (2005).
- [40] A. Armaou, I. G. Kevrekidis, and C. Theodoropoulos, Equation-free gaptooth-based controller design for distributed complex/multiscale processes, *Computers & chemical engineering* **29**, 731 (2005).
- [41] E. Galaris, G. Fabiani, I. Gallos, I. Kevrekidis, and C. Siettos, Numerical bifurcation analysis of pdes from lattice boltzmann model simulations: a parsimonious machine learning approach, *Journal of Scientific Computing* **92**, 34 (2022).
- [42] G. A. Pavliotis and A. Zannoni, A method of moments estimator for interacting particle systems and their mean field limit (2022), *arXiv:2212.00403 [math.NA]*.
- [43] P.-H. Chavanis, The Brownian mean field model, *Eur. Phys. J. B* **87**, Art. 120, 33 (2014).
- [44] D. S. Dean, Langevin equation for the density of a system of interacting langevin processes, *Journal of Physics A: Mathematical and General* **29**, L613 (1996).
- [45] K. Kawasaki, Microscopic analyses of the dynamical density functional equation of dense fluids, *Journal of statistical physics* **93**, 527 (1998).
- [46] N. Evangelou, F. Dietrich, E. Chiavazzo, D. Lehmberg, M. Meila, and I. G. Kevrekidis, Double diffusion maps and their latent harmonics for scientific computations in latent space, *Journal of Computational Physics* **485**, 112072 (2023).
- [47] C. Fowlkes, S. Belongie, F. Chung, and J. Malik, Spectral grouping using the nystrom method, *IEEE transactions on pattern analysis and machine intelligence* **26**, 214 (2004).
- [48] A. Paszke, S. Gross, F. Massa, A. Lerer, J. Bradbury, G. Chanan, T. Killeen, Z. Lin, N. Gimelshein, L. Antiga, A. Desmaison, A. Kopf, E. Yang, Z. DeVito, M. Raison, A. Tejani, S. Chilamkurthy, B. Steiner, L. Fang, J. Bai, and S. Chintala, Pytorch: An imperative style, high-performance deep learning library, in *Advances in Neural Information Processing Systems 32* (Curran Associates, Inc., 2019) pp. 8024–8035.
- [49] M. Abadi, A. Agarwal, P. Barham, E. Brevdo, Z. Chen, C. Citro, G. S. Corrado, A. Davis, J. Dean, M. Devin, S. Ghemawat, I. Goodfellow, A. Harp, G. Irving, M. Isard, Y. Jia, R. Jozefowicz, L. Kaiser, M. Kudlur, J. Levenberg, D. Mané, R. Monga, S. Moore, D. Murray, C. Olah, M. Schuster, J. Shlens, B. Steiner, I. Sutskever, K. Talwar, P. Tucker, V. Vanhoucke, V. Vasudevan, F. Viégas, O. Vinyals, P. Warden, M. Wattenberg, M. Wicke, Y. Yu, and X. Zheng, TensorFlow: Large-scale machine learning on heterogeneous systems (2015), software available from tensorflow.org.